ChemComm

COMMUNICATION

View Article Online
View Journal

Cite this: DOI: 10.1039/d2cc02671f

Received 10th May 2022,
Accepted 20th June 2022

DOI: 10.1039/d2cc02671f

rsc.li/chemcomm

Boosting the catalytic performance of single-atom catalysts by tuning surface lattice expanding confinement†

Fei Gao, ‡*[a] Annai Liu,‡[b] Wei Tan,‡[a] Bing Hu,[c] Ruihan Gong,[a] Xing Cheng,[d] Fudong Liu,[e] Ge Chen [d] and Lin Dong [a]

A Ti^{3+}-rich rutile TiO_2 with a surface lattice expansion structure was constructed by H_2 treatment, on which the supported Pt single atoms were stabilized in a highly oxidized state under a CO oxidation reaction atmosphere and had a weaker affinity for CO, thus exhibiting robust catalytic performance.

Increasing the metal dispersion by decreasing the size of noble metal particles is one of the most promising ways to lower the cost of noble-metal catalysts for practical applications.[1,2] Another critical motivation for studying highly dispersed metal catalysts is to explore the novel catalytic behavior associated with the subnanometric metal species, including single atoms (SAs) and small metal clusters.[3–8] Despite the increasing publications, there are some arguments on the working active sites in single-atom catalysts (SACs).[9] For instance, it is claimed by some researchers that Pt SAs surpass conventional nanoparticles for catalytic CO oxidation,[10,11] while others insisted that clusters or nanoparticles are the real active sites.[12–15]

To address the reaction mechanism and the nature of active sites, one has to consider various factors that may influence the catalytic behavior/stability of SAs. By translating the lessons learnt from systems based on metal nanoparticles into SAs,[16–21] we expect that the surface properties/structures of the oxide supports should have a profound influence on the catalytic behavior of SAs.[13,22,23] From a structural point of view, the solid carriers influence the catalytic performance of the supported SAs through modulating their coordination environment, which could be the key to the comprehension and modification of single-atom catalysis.[24–26] In this work, it is demonstrated that the electron deficiency and coordination environments of the supported Pt SAs could be tuned through engineering the TiO_2 surfaces, resulting in the change of adsorption/desorption behaviors of Pt SAs to reactants (CO and O_2), and thus improving the CO oxidation activity.

Using a previously reported H_2-treatment method at 873 K,[27] reduced surfaces with rich Ti^{3+} on rutile TiO_2 nanoparticles were constructed. The degree of surface reduction was controlled by varying the partial pressure of H_2. According to the color of the powder (Fig. S1, ESI†), the reduced and highly reduced TiO_2 samples are labeled as TiO_2-Gr (Gr means "grey") and TiO_2-Dg (Dg means "dark grey"), respectively. Rutile powder treated at 873 K in air was used as the non-reduced reference support, denoted as TiO_2-Wt. Although there are numerous works on the structures of reduced TiO_2, the detailed features of the surfaces of reduced TiO_2 materials are not clearly revealed at an atomic level.[28–30] According to the results of transmission electron microscopy (TEM, Fig. S2, ESI†) and X-ray diffraction (XRD, Fig. S3, ESI†), the pre-reduction treatment generally did not affect the particle size or the morphology of the rutile nanocrystals, which was also evidenced by the barely changed BET surface area (23–24 $m^2\ g^{-1}$ for all samples). Therefore, the pre-reduction treatment mainly influences the surface properties of the rutile nanocrystals. For TiO_2-Wt (Fig. 1(A)), the distance of lattice fringes near the surface region is identical to that in the bulk region (2.5 Å). For the reduced samples, however, the lattices near the edge are larger than the bulk phase (Fig. 1(B) and (C)) and the surface lattice near the edge on TiO_2-Dg (2.7 Å) is even larger than that on TiO_2-Gr (2.6 Å). These observations demonstrate the changes in the crystalline structure of the TiO_2 surface after H_2 treatment.

[a] State Key Laboratory of Pollution Control and Resource Reuse, School of Environment, Jiangsu Key Laboratory of Vehicle Emissions Control, Center of Modern Analysis, Key Laboratory of Mesoscopic Chemistry of MOE, School of Chemistry and Chemical Engineering, Nanjing University, Nanjing 210023, China. E-mail: gaofei@nju.edu.cn
[b] Institute of Engineering Technology, Sinopec Catalyst Co. Ltd., Sinopec Group, 13 Xingguang 5th Avenue, Beijing 101111, P. R. China
[c] Institute for Catalysis, Hokkaido University, Kita 21 Nishi 10, Kita-ku, Sapporo, Hokkaido 001-0021, Japan
[d] College of Environmental and Energy Engineering, Beijing University of Technology, Pingle yuan 100, Beijing 100124, P. R. China
[e] Department of Civil, Environmental, and Construction Engineering, Catalysis Cluster for Renewable Energy and Chemical Transformations (REACT), NanoScience Technology Center (NSTC), University of Central Florida, Orlando, FL 32816, USA

† Electronic supplementary information (ESI) available: Details of methods, digital photographs, BF-TEM images, XRD, Raman, XANES, and EXAFS spectra, simulated TiO_2 structures, Arrhenius plots, CO_{ad}-TPO and DFT. See DOI: https://doi.org/10.1039/d2cc02671f

‡ These authors contributed equally.

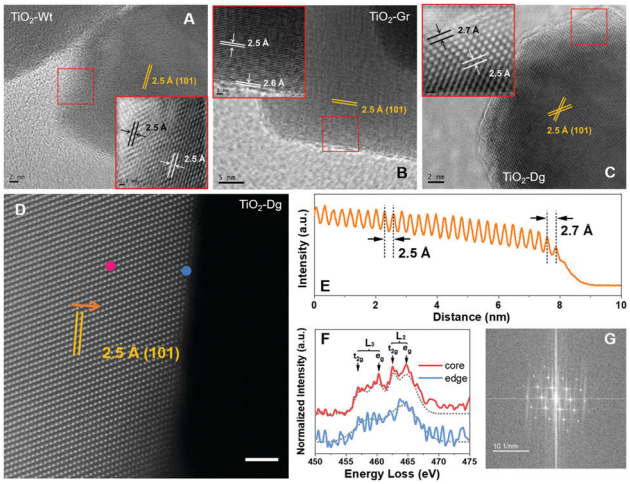

Fig. 1 (A)–(C) High-resolution TEM images of TiO_2-Wt (A), TiO_2-Gr (B), and TiO_2-Dg (C), insets magnifying the selected parts in red squares from the corresponding images. (D) The AC-STEM-HAADF image of TiO_2-Dg (scale bar: 2 nm), inset showing the simulated reduced surface structure of rutile (101). (E) The line profile of intensity along the arrow in D. (F) The EELS spectra of 2 spots from the edge (pink) and the core (blue) of the same TiO_2 nanocrystal in D. (G) The FFT pattern of the corresponding region in (D) of the TiO_2-Dg sample.

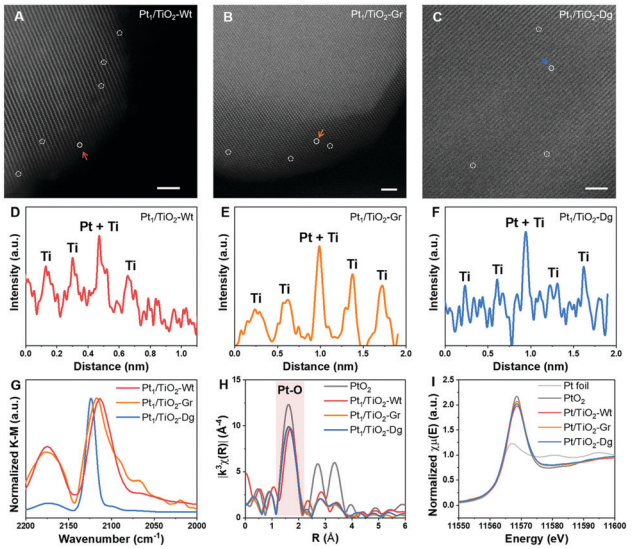

Fig. 2 (A)–(C) The AC-STEM-HAADF images of Pt_1/TiO_2-Wt(A), Pt_1/TiO_2-Gr(B), and Pt_1/TiO_2-Dg(C), in which some Pt atoms are circled (scale bar: 2 nm). (D)–(F) Line profiles of scattered electron intensities along the arrows in the corresponding HAADF images. (G) *In situ* DRIFT of CO oxidation on all 3 samples at 373 K (gas feed 1% CO, 1% O_2, and He balance). (H and I) EXAFS (H) and XANES (I) of Pt_1/TiO_2 samples with Pt and PtO_2 as references.

We further investigated TiO_2-Dg by aberration-corrected STEM in the high-angle annular dark-field mode (AC-STEM-HAADF) along with electron energy loss spectroscopy (EELS). The expansion of the surface lattice is also confirmed using the AC-STEM-HAADF images (Fig. 1(D) and (E)). Moreover, as shown in Fig. 1(F), the four peaks in the EELS spectrum of bulk spot (pink) could be divided into 2 groups, Ti-L_3 and Ti-L_2, indicating a typical rutile TiO_2 structure. However, the 2 broad peaks in the EELS spectrum of the edge spot (blue) are ascribed to the signal of Ti^{3+} species.[31,32] Various spectroscopic characterization methods (XAFS, EPR, and Raman, Fig. S4–S10 and Table S1, ESI†) further confirmed the presence of the surface lattice expansion with a slight decrease of the periodicity and Ti^{3+} on reduced TiO_2 surfaces. Density functional theory (DFT) calculations suggested that the surface crystalline lattice expansion is caused by the formation of Ti^{3+} (67 pm) with a larger ionic radius than Ti^{4+} (60.5 pm) (Fig. S11, ESI†).

To study the catalytic behavior of the supported active species potentially influenced by surface geometries and electronic structures, Pt SAs (0.1 wt%) were deposited on different TiO_2 surfaces *via* a wetness impregnation method. As shown in Fig. 2(A)–(C), Pt SAs are observed as bright dots in the AC-STEM-HAADF images, confirmed by the corresponding contrast profiles (Fig. 2(D)–(F)). Moreover, the positions of Pt_1 matched well with the columns of Ti atoms, suggesting that Pt should be located at the substitution sites or epitaxial growth sites of Ti ions on the TiO_2 surface. According to the results of *in situ* diffuse reflectance infrared Fourier transform spectroscopy (DRIFTS) with CO as the probe molecule (CO oxidation atmosphere at 373 K, Fig. 2(G)), the CO adsorption bands are at 2130–2110 cm^{-1} in all three samples, which are ascribed to mono-carbonyl species linearly adsorbed on isolated $Pt^{\delta+}$ atoms.[33] The varied positions of CO IR bands on Pt_1/TiO_2-Wt, Pt_1/TiO_2-Gr and Pt_1/TiO_2-Dg hinted at the different valence states and coordination environments of Pt_1 on different TiO_2 supports. It was also noticeable that the full width at half maximum (FWHM) of these CO IR bands were different. The well-defined CO IR band with high symmetry on Pt_1/TiO_2-Dg indicated the uniform states of Pt_1, which could be related to Pt anchored on the same sites induced by the Ti^{3+}/surface defects, *i.e.*, the reaction between the reduced TiO_2 surface and Pt-O_x/Pt-$(OH)_x$ could help strongly anchor the Pt atoms. As illustrated by Pt-L_3 edge EXAFS (Fig. 2(H), Fig. S13–S15 and Table S2, ESI†), there is only one dominant coordination shell of Pt–O for all three samples, suggesting that Pt species are in the single-atom form. It was also revealed that the Ti–O distance was 1.95 Å (Table S1, ESI†) and the average Pt–O distances on Pt_1/TiO_2-Wt, Pt_1/TiO_2-Gr and Pt_1/TiO_2-Dg were *ca.* 2.05, 2.02 and 2.02 Å (Table S2, ESI†), respectively. With the increase in the degree of surface reduction of TiO_2 supports, the average Pt–O distance decreased from 2.05 to 2.02 Å, suggesting the stronger confinement of Pt atoms within the reduced TiO_2 samples.

Then the catalytic performance of the prepared Pt_1/TiO_2 samples in the CO oxidation reaction at 373 K was evaluated. As listed in Table 1, compared to Pt_1/TiO_2-Wt, Pt SAs supported on reduced TiO_2 exhibited significantly enhanced activities. The apparent activation energies of Pt_1/TiO_2-Dg and Pt_1/TiO_2-Gr are also lower than that of Pt_1/TiO_2-Wt (Fig. S12, ESI†), confirming the higher CO oxidation activity on Pt SAs supported on the reduced TiO_2. Pt_1/TiO_2-Dg also exhibited one of the most outstanding CO oxidation activities among those recently reported SACs.

Detailed characterization on Pt_1/TiO_2 samples and DFT calculations were performed to reveal the reasons for their

Table 1 The CO oxidation activity of Pt_1/TiO_2 samples

Samples	Reaction rate at 373 K $\times$ 10^2 (mol_{CO} mol_{Pt}^{-1} s^{-1})[a]	E_{app} (kJ mol^{-1})	Ref.
Pt_1/TiO_2-Wt	0.80 $\pm$ 0.01	42.1 $\pm$ 1.5	
Pt_1/TiO_2-Gr	1.49 $\pm$ 0.05	30.9 $\pm$ 1.1	
Pt_1/TiO_2-Dg	3.48 $\pm$ 0.12	28.7 $\pm$ 1.8	
Pt_1/TiO_2	2.12 (433 K)	68.5	34
Pt_1/KLTL	1.20 (423 K)	—	10
Pt_1/θ-Al_2O_3	1.3 (473 K)	—	35
Pt_1/CeO_2	0.60	42.5	36

different catalytic performances. As demonstrated in Fig. 2(G), the positions of CO band centers follow the order of CO-Pt_1/TiO_2-Dg > CO-Pt_1/TiO_2-Gr > CO-Pt_1/TiO_2-Wt, indicating a more significant electron deficiency for Pt single atoms on the reduced surfaces, leading to the higher valence of Pt, well supported by Pt-L_3 edge XANES (Fig. 2(I)). This stronger interaction between Pt_1 and the reduced TiO_2 surface could be better illustrated with the CO_{ad}-TPO test by *in situ* DRIFTS (Fig. S16, ESI†) revealing that the Pt_1 anchored on TiO_2-Dg was rather stable and exhibit a high electron deficit even at high temperatures. The high stability of Pt_1 on TiO_2-Dg was also well proved by *in situ* DRIFTS of CO adsorption on used samples after the CO oxidation test (Fig. S17, ESI†).

As discussed above, Pt_1 with high electron deficiency stabilized by reduced TiO_2 might play a key role in the catalytic process at low temperatures. To further understand the nature of Pt sites theoretically, we computed the structures of Pt atoms supported on perfect and reduced rutile TiO_2 (101) surfaces, denoted as Pt_1/perfect TiO_2 (S1) and Pt_1/reduced TiO_2 (S2), respectively. As depicted in Fig. 3(A), for Pt_1/perfect TiO_2, the Pt atom is bonded to the surface oxygen atoms (S1). For Pt_1/reduced TiO_2 (S2), based on the observation that Pt SAs on reduced TiO_2 support were confined by the expanded surface lattice, we constructed a structural model in which a Ti atom near the oxygen vacancy was replaced by a Pt atom (S2, Fig. 3(B)), which was also proposed in previous studies.[37] The calculated formation energy of isolated Pt atoms at the Ti site (S2, 1.12 eV) is far less than that of Pt atoms on the perfect TiO_2 surface (S1, 2.43 eV), suggesting that the break of surface periodicity and expansion of surface lattice (TiO_2-Gr and TiO_2-Dg) can benefit the substitution of Ti atoms by Pt atoms. The lower formation energy of the S2 structure is potentially related to higher stability, in accordance with the CO_{ad}-TPO results (Fig. S16, ESI†). To better illustrate the structural properties of Pt SAs in S1 and S2, the electron localization function is also computed (Fig. 3(C) and (D)), and a stronger interaction between Pt and O atoms for S2 can be concluded from the higher electron deficiency of Pt (+1.13 higher charge transfer) at the interface of Pt–O. Moreover, compared to S1, higher adsorption energy of O_2 and lower activation energy of the O–O dissociation are achieved on Pt atoms in S2 (Fig. S18, ESI†). These findings indicate the stronger interaction between O atoms and Pt SAs supported on reduced TiO_2 surfaces, consistent with the XAFS results.

The different apparent activation energies of all three samples (Table 1 and Fig. S12 (ESI†), Pt_1/TiO_2-Dg < Pt_1/TiO_2-Gr < Pt_1/TiO_2-Wt) indicated that the reaction pathways of catalytic CO oxidation might vary on Pt SAs with different coordination environments. Considering the strong adsorption of CO molecules on Pt species at low temperatures and previous reports,[36,38] CO oxidation on Pt SAs following the Langmuir–Hinshelwood (L–H) mechanism was simulated first (Fig. 4). For Pt atoms supported on perfect TiO_2 (S1), after the adsorption of CO on Pt, substantial distortion (TS1) was observed with a relatively high adsorption energy (−2.69 eV), in line with the previous reports.[13] This strong adsorption hinders the following reaction with adsorbed oxygen. As a result, Pt_1/TiO_2-Wt will exhibit limited CO oxidation activity *via* the L–H pathway. However, for Pt atoms anchored on reduced TiO_2 (S2), the adsorption energy of CO decreased remarkably, which facilitates the reaction between adsorbed CO and adsorbed oxygen, evidenced by the lower energy barrier. Moreover, we also tested another pathway, in which adsorbed CO molecules react with lattice oxygen directly, known as the Mars-van Krevelen (MvK) mechanism.[39,40] With a little decrease of the energy barrier for S1 (Fig. S19, ESI†), the results still show that Pt SAs in the S2 configuration under the L–H pathway are more favorable. In short, for Pt SAs supported on TiO_2 surfaces, the CO oxidation follows either the L–H or the MvK pathway, depending on the chemical environment of Pt atoms, and the determining step is the reaction of strongly adsorbed CO with activated oxygen. That is, Pt SAs on reduced TiO_2 with higher electron deficiency would suppress the strong CO adsorption, which is the key to higher CO oxidation activity.

In summary, we have investigated the effect of surface engineering on the rutile TiO_2 *via* H_2-reduction at high temperatures. The reduced TiO_2 with abundant Ti^{3+} and surface lattice expansion structures can induce the formation of Pt SAs with high electron deficiency and stability, which leads to weaker CO adsorption and facilitates further reactions between

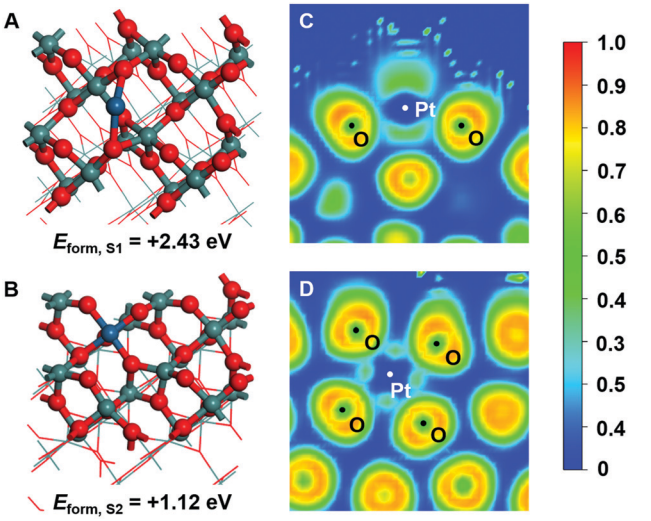

Fig. 3 The simulated structures of S1 (A) and S2 (B). Blue, green, and red balls indicate Pt, Ti, and O atoms, respectively. The electron localization function analysis of the corresponding Pt_1/TiO_2 structures (C for S1 and D for S2).

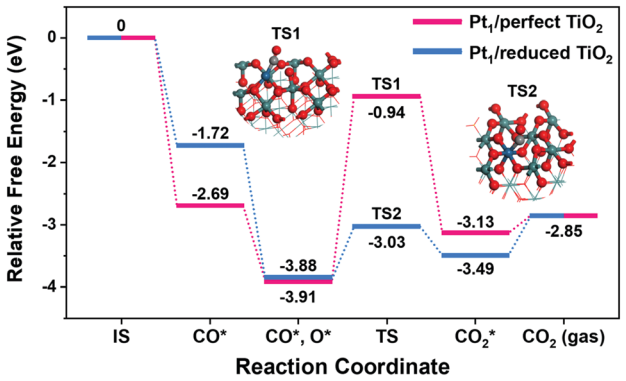

Fig. 4 The energy diagram of CO oxidation on Pt_1/perfect TiO_2 (pink) and Pt_1/reduced TiO_2 (blue) at 373 K *via* the Langmuir–Hinshelwood mechanism. All pathways are corrected to free energy. Blue, green, gray, and red balls indicate Pt, Ti, C, and O atoms, respectively.

adsorbed CO and activated O species. This work sets forth an example of how structural changes can tune the electronic properties and the coordination environment of supported single atoms, ultimately boosting their catalytic activity. The idea of surface structural modification of the catalyst carriers provides new insights into understanding the performance of SACs and ways to improve them.

B. Hu, R. Gong, X. Cheng, F. Liu and G. Chen helped in performing the catalyst preparation and characterization. Prof. F. Gao, Prof. L. Dong and Dr A. Liu designed this study. Dr A. Liu and Dr W. Tan analyzed the data and wrote the manuscript.

This work was supported by the National Natural Science Foundation of China (No. 21972063) and the Natural Science Foundation of Jiangsu Province (BK20200012). We thank Dr Meiyu Wang at Sub-atomic Resolution Electron Microscopy Laboratory at Nanjing University for the STEM imaging and data analysis.

Conflicts of interest

There are no conflicts of interest to declare.

Notes and references

1 L. Liu and A. Corma, *Chem. Rev.*, 2018, **118**, 4981–5079.
2 X. Li, X. Yang, Y. Huang, T. Zhang and B. Liu, *Adv. Mater.*, 2019, **31**, 1902031.
3 J. Liu, Catalysis by Supported Single Metal Atoms, *ACS Catal.*, 2017, **7**, 34–59.
4 A. Wang, J. Li and T. Zhang, Heterogeneous Single-Atom Catalysis, *Nat. Rev. Chem.*, 2018, **2**, 65–81.
5 Z. Li, S. Ji, Y. Liu, X. Cao, S. Tian, Y. Chen, Z. Niu and Y. Li, *Chem. Rev.*, 2020, **120**, 623–682.
6 N. Zhang, C. Ye, H. Yan, L. Li, H. He, D. Wang and Y. Li, *Nano Res.*, 2020, **13**, 3165–3182.
7 Y. Guo, S. Mei, K. Yuan, D.-J. Wang, H.-C. Liu, C.-H. Yan and Y.-W. Zhang, *ACS Catal.*, 2018, **8**, 6203–6215.
8 Y. Lou, Y. Cai, W. Hu, L. Wang, Q. Dai, W. Zhan, Y. Guo, P. Hu, X.-M. Cao, J. Liu and Y. Guo, *ACS Catal.*, 2020, **10**, 6094–6101.
9 L. Liu, D. M. Meira, R. Arenal, P. Concepcion, A. V. Puga and A. Corma, *ACS Catal.*, 2019, **9**, 10626–10639.
10 J. D. Kistler, N. Chotigkrai, P. Xu, B. Enderle, P. Praserthdam, C. Y. Chen, N. D. Browning and B. C. Gates, *Angew. Chem., Int. Ed.*, 2014, **53**, 8904–8907.
11 B. Qiao, A. Wang, X. Yang, L. F. Allard, Z. Jiang, Y. Cui, J. Liu, J. Li and T. Zhang, *Nat. Chem.*, 2011, **3**, 634–641.
12 Z. Li, S. Dai, L. Ma, Z. Qu, N. Yan and J. Li, *Chem. Eng. J.*, 2021, **413**, 127447.
13 K. Ding, A. Gulec, A. M. Johnson, N. M. Schweitzer, G. D. Stucky, L. D. Marks and P. C. Stair, *Science*, 2015, **350**, 189–192.
14 H. Jeong, O. Kwon, B.-S. Kim, J. Bae, S. Shin, H.-E. Kim, J. Kim and H. Lee, *Nat. Catal.*, 2020, **3**, 368–375.
15 K. Yuan, Y. Guo, Q.-L. Lin, L. Huang, J.-T. Ren, H.-C. Liu, C.-H. Yan and Y.-W. Zhang, *J. Catal.*, 2021, **394**, 121–130.
16 Z. Wu, Y. Li and W. Huang, *J. Phys. Chem. Lett.*, 2020, **11**, 4603–4607.
17 S. Chen, L. Luo, Z. Jiang and W. Huang, *ACS Catal.*, 2015, **5**, 1653–1662.
18 X.-Q. Gong, A. Selloni, O. Dulub, P. Jacobson and U. Diebold, *J. Am. Chem. Soc.*, 2008, **130**, 370–381.
19 J. Saavedra, H. A. Doan, C. J. Pursell, L. C. Grabow and B. D. Chandler, *Science*, 2014, **345**, 1599–1602.
20 J. Ke, W. Zhu, Y. Jiang, R. Si, Y.-J. Wang, S.-C. Li, C. Jin, H. Liu, W.-G. Song, C.-H. Yan and Y.-W. Zhang, *ACS Catal.*, 2015, **9**, 5164–5173.
21 S. Song, Y. Wu, S. Ge, L. Wang, Y. Wang, Y. Guo, W. Zhan and Y. Guo, *ACS Catal.*, 2019, **9**, 6177–6187.
22 Z. Hu, Z. Wang, Y. Guo, L. Wang, Y. Guo, J. Zhang and W. Zhan, *Angew. Chem., Int. Ed.*, 2018, **57**, 9351–9356.
23 Z. Jiang, M. Jing, X. Feng, J. Xiong, C. He, M. Douthwaite, L. Zheng, W. Song, J. Liu and Z. Qu, *Appl. Catal., B*, 2020, **278**, 119304.
24 X. Li, X. Huang, S. Xi, S. Miao, J. Ding, W. Cai, S. Liu, X. Yang, H. Yang, J. Gao, J. Wang, Y. Huang, T. Zhang and B. Liu, *J. Am. Chem. Soc.*, 2018, **140**, 12469–12475.
25 R. Qin, K. Liu, Q. Wu and N. Zheng, *Chem. Rev.*, 2020, **120**, 11810–11899.
26 Y. Chen, S. Ji, Y. Wang, J. Dong, W. Chen, Z. Li, R. Shen, L. Zheng, Z. Zhuang, D. Wang and Y. Li, *Angew. Chem., Int. Ed.*, 2017, **56**, 6937–6941.
27 A. Naldoni, M. Allieta, S. Santangelo, M. Marelli, F. Fabbri, S. Cappelli, C. L. Bianchi, R. Psaro and V. Dal Santo, *J. Am. Chem. Soc.*, 2012, **134**, 7600–7603.
28 X. Chen, L. Liu and F. Huang, *Chem. Soc. Rev.*, 2015, **44**, 1861–1885.
29 S. G. Ullattil, S. B. Narendranath, S. C. Pillai and P. Periyat, *Chem. Eng. J.*, 2018, **343**, 708–736.
30 A. Naldoni, M. Altomare, G. Zoppellaro, N. Liu, Š. Kment, R. Zbořil and P. Schmuki, *ACS Catal.*, 2019, **9**, 345–364.
31 M. Tian, M. Mahjouri-Samani, G. Eres, R. Sachan, M. Yoon, M. F. Chisholm, K. Wang, A. A. Puretzky, C. M. Rouleau, D. B. Geohegan and G. Duscher, *ACS Nano*, 2015, **9**, 10482–10488.
32 J. Lim, S.-H. Kim, R. Aymerich Armengol, O. Kasian, P.-P. Choi, L. T. Stephenson, B. Gault and C. Scheu, *Angew. Chem., Int. Ed.*, 2020, **59**, 5651–5655.
33 B. Han, Y. Guo, Y. Huang, W. Xi, J. Xu, J. Luo, H. Qi, Y. Ren, X. Liu, B. Qiao and T. Zhang, *Angew. Chem., Int. Ed.*, 2020, **59**, 11824–11829.
34 L. DeRita, S. Dai, K. Lopez-Zepeda, N. Pham, G. W. Graham, X. Pan and P. Christopher, *J. Am. Chem. Soc.*, 2017, **139**, 14150–14165.
35 M. Moses-DeBusk, M. Yoon, L. F. Allard, D. R. Mullins, Z. Wu, X. Yang, G. Veith, G. M. Stocks and C. K. Narula, *J. Am. Chem. Soc.*, 2013, **135**, 12634–12645.
36 L. Nie, D. Mei, H. Xiong, B. Peng, Z. Ren, X. I. P. Hernandez, A. DeLaRiva, M. Wang, M. H. Engelhard and L. Kovarik, *Science*, 2017, **358**, 1419–1423.
37 H. V. Thang, G. Pacchioni, L. DeRita and P. Christopher, *J. Catal.*, 2018, **367**, 104–114.
38 T. Kropp, Z. Lu, Z. Li, Y.-H. C. Chin and M. Mavrikakis, *ACS Catal.*, 2019, **9**, 1595–1604.
39 C. Wang, X.-K. Gu, H. Yan, Y. Lin, J. Li, D. Liu, W.-X. Li and J. Lu, *ACS Catal.*, 2017, **7**, 887–891.
40 A. J. Therrien, A. J. R. Hensley, M. D. Marcinkowski, R. Zhang, F. R. Lucci, B. Coughlin, A. C. Schilling, J.-S. McEwen and E. C. H. Sykes, *Nat. Catal.*, 2018, **1**, 192–198.

